Path-Conservative Central-Upwind Schemes for the Non-Conservative NET-RAT Traffic Flow Model

Saeed Mohammadian[a], Zuduo Zheng[a,*], Shaoshuai Chu[b], Alexander Kurganov[c]

[a]*School of Civil Engineering, the University of Queensland, Brisbane Qld, 4072, Australia*
[b]*Department of Mathematics and Shenzhen International Center for Mathematics, Southern University of Science and Technology, Shenzhen, 518055, China*
[c]*Department of Mathematics and Shenzhen International Center for Mathematics, Southern University of Science and Technology and Guangdong Provincial Key Laboratory of Computational Science and Material Design, Southern University of Science and Technology, Shenzhen, 518055, China*

Abstract

Behavioral non-equilibrium hyperbolic traffic models, derived from approximated car-following models with human factors, can lose their conservative form, rendering traditional flux-based numerical methods ineffective. This challenge also applies to the recently proposed behavioral continuum (non-equilibrium traffic model based on risk allostasis theory, that is, NET-RAT) model. This paper is focused on solving the Riemann problem and several other initial-value problems for the novel NET-RAT model in the non-conservative form, by developing path-conservative central-upwind (PCCU) schemes. In order to examine performance of the proposed PCCU schemes, we design extensive numerical tests considering the unique behavioral properties of the NET-RAT model. The PCCU schemes are then applied to these tests and the obtained results demonstrate that major wave types are effectively and accurately captured. At the same time, the fifth-order scheme, which is constructed using an alternative weighted essentially non-oscillatory (A-WENO) approach yields substantially sharper resolution than its second-order counterpart. The proposed schemes can facilitate the practical implementation of the NET-RAT model for real-world traffic.

Keywords: Traffic flow theory; behavioral non-equilibrium hyperbolic traffic flow models; non-equilibrium traffic model based on risk allostasis theory (NET-RAT) model; path-conservative central-upwind schemes; A-WENO schemes

This research was partially funded by the Australian Research Council (ARC) through the Discover Project (DP210102970) and Dr. Zuduo Zheng's Discovery Early Career Researcher Award (DECRA; DE160100449). The work of A. Kurganov was supported in part by NSFC grant 12171226 and by the fund of the Guangdong Provincial Key Laboratory of Computational Science and Material Design (No. 2019B030301001).

1. Introduction

Continuum traffic flow models use aggregated variables to describe traffic dynamics as a compressible fluid. These models are formulated as hyperbolic systems of partial differential equations (PDEs), allowing the determination of state variables over time and space based on initial and boundary conditions [29]. These models find applications in short-term traffic prediction, congestion propagation, freeway and network optimizations, and the study of complex traffic phenomena [see, e.g., 26, 31]. Over time, numerous continuum models have been proposed to incorporate various behavioral and empirical aspects of traffic flow; we refer the reader to [25] and [24] for a detailed review and performance analysis for real-world traffic flows.

In contrast to many physical systems, traffic flow is heavily influenced by real-time decision-making processes of human drivers [11]. These processes are governed by psychological factors that shape their perception of traffic conditions. Several empirical studies have established strong connections between these human factors and complex traffic phenomena, such as hysteresis and traffic instabilities [2, 27], highlighting

*Corresponding author
Email addresses: s.mohammadian@uq.edu.au (Saeed Mohammadian), z.zheng@uq.edu.au (Zuduo Zheng), chuss@mail.sustech.edu.cn (Shaoshuai Chu), kurganov@math.sc.edu (Alexander Kurganov)

the importance of developing improved behavioral models that can effectively incorporate the impact of these factors.

From a macroscopic standpoint, a relevant question would be to examine how such microscopic behavioral processes influence collective characteristics of traffic flow, including wave propagation and stability. Exploring such aspects involves integrating human factors into a well-defined car-following model and then deriving a behavioral macroscopic model that serves as the corresponding continuum "equivalent" [16]. Well-defined behavioral continuum models are, however, notably rare in the literature of macroscopic traffic flow models. This scarcity can be attributed to the requirement of incorporating a comprehensive theory of human driving factors into the foundational assumptions of the car-following model. As a result, the development of complex behavioral mechanisms is likely to compromise the conservative nature of the hyperbolic equations in the resulting continuum model [20]. Consequently, classical numerical methods that rely on numerical fluxes (see, e.g., [15, 19, 22]) cannot be applied to study Riemann problems in this context and, in general, to capture discontinuous solutions of the considered non-conservative models [32]. In other words, the presence of numerical challenges might have hindered the development of complex behavioral continuum models, highlighting the importance of addressing this research gap.

Motivated by an attempt to close the research gap, a novel behavioral continuum model, known as NET-RAT (Non-Equilibrium Traffic model based on Risk Allostasis Theory), has been developed in [23]. NET-RAT is a parsimonious "second-order" continuum model that incorporates drivers' dynamic response adaptation process in relation to their perceived risk through car-following processes. This model effectively associates the emergence of complex traffic phenomena (such as hysteresis and traffic instabilities) with the interplay between drivers' dynamic adaptation process and their perceived car-following risk. NET-RAT's rule-based and switching logic, along with its intricate behavioral adaptation mechanisms, prevent its governing equations from being expressed explicitly in a conservative form. Therefore, the NET-RAT model has the same numerical limitations as the other aforementioned non-conservative traffic flow models [19, 22].

This paper focuses on the development of robust and accurate numerical methods for the NET-RAT traffic flow model. In order to overcome the difficulties associated with the lack of conservation, we adopt the path-conservative approach and, as in our recent work [3], develop path-conservative central-upwind (PCCU) schemes for the NET-RAT model. We first derive a second-order finite-volume (FV) PCCU scheme and then extend it to the fifth-order of accuracy through the finite-difference (FD) alternative weighted essentially non-oscillatory (A-WENO) framework. Extensive numerical tests, considering the unique behavioral characteristics of NET-RAT, are designed in order to assess the proposed schemes. The obtained results demonstrate that major wave types are effectively and accurately captured. At the same time, the fifth-order A-WENO scheme leads to a substantially higher resolution compared with its second-order counterpart.

The rest of the paper is organized as follows. Section 2 provides an overview of the NET-RAT model. Section 3 presents the proposed PCCU schemes. Section 4 contains the study design, results, and discussions, which cover various aspects such as numerical tests, parameter setup, and the performance evaluation of the proposed numerical methods. Finally, Section 5 presents the concluding remarks.

2. The Behavioral NET-RAT Traffic Model

The novel continuum NET-RAT model has recently been developed in [23]. This model is derived from extending the full velocity difference car-following model [13], where the driver sensitivity is extended to be dynamically dependent on the perceived risk, which is modeled based on the proportion of the stopping distance [see, e.g., 21]. The interactions between perceived risk and driver sensitivity are further modeled based on the risk allostasis theory [7]. For a more detailed discussion on the derivation processes from car-following relations, we refer the reader to [23].

The NET-RAT model for a section of a homogeneous road in its hyperbolic form reads as

$$\begin{cases} \rho_t + (\rho V)_x = 0, \\ V_t + VV_x = \dfrac{V_e(\rho) - V}{T_{\text{relax}}} - \psi(\mathfrak{R}_{\text{perc}})C(\rho)V_x. \end{cases} \tag{1}$$

Here, x is the spatial variable, t is time, ρ is the traffic density, V is the speed, $V_e(\rho)$ denotes the equilibrium speed or the fundamental diagram, and T_{relax} is the relaxation time. The specific formulation for $V_e(\rho)$ is provided in [5] and it reads as

$$V_e(\rho) = \frac{C_{\text{jam}}}{\widetilde{\rho}}\Big[1 + (a-1)\widetilde{\rho} - \big((a\widetilde{\rho})^\theta + (1-\widetilde{\rho})^\theta\big)^{\frac{1}{\theta}}\Big],$$

where $\widetilde{\rho} := \rho/\rho_{\max}$ represents the normalized traffic density, $a := V_{\max}/C_{\rm jam}$ denotes the ratio of the maximum speed to the magnitude of jam, $C_{\rm jam}$, which corresponds to the magnitude of the propagation velocity $\lambda_* = V_e(\rho) + C(\rho)$ under the jam condition when the density is at its maximum ($\rho = \rho_{\max}$), and $\theta \in (1, \infty)$ serves as a shape parameter. Moreover, in (1), $C(\rho) = \rho V_e'(\rho)$ indicates the relative rate at which smooth variations in the traffic density profile propagate, as observed by a moving observer traveling at the average traffic speed if $\psi(\mathfrak{R}_{\rm perc}) = 1$, and $\psi(\mathfrak{R}_{\rm perc})$ takes into account the influence of drivers' perceived risk on their sensitivity and, consequently, on the propagation velocity of disturbances. This function is defined as a function of speed density as

$$\psi(\mathfrak{R}_{perc}) = \begin{cases} 1 - \gamma_1\left(\dfrac{\mathfrak{L}_{\rm arr} - \mathfrak{R}_{\rm perc}}{\mathfrak{L}_{\rm arr}}\right) & \text{if } \mathfrak{R}_{\rm perc} < \mathfrak{L}_{\rm arr}, \\ 1 & \text{if } \mathfrak{L}_{\rm arr} \le \mathfrak{R}_{\rm perc} \le \mathfrak{U}_{\rm arr}, \\ 1 + \gamma_2\left(\dfrac{\mathfrak{R}_{\rm perc} - \mathfrak{U}_{\rm arr}}{\mathfrak{R}_{\rm perc}}\right) & \text{if } \mathfrak{R}_{\rm perc} > \mathfrak{U}_{\rm arr}, \end{cases}$$

where $\mathfrak{R}_{\rm perc}$ is the perceived risk, defined by

$$\mathfrak{R}_{\rm perc} = \begin{cases} \dfrac{1}{\rm PSD_{min}} & \text{if } \mu_{\rm PSD}(x,t) < {\rm PSD_{min}}, \\ \dfrac{1}{\rm PSD_{max}} & \text{if } \mu_{\rm PSD}(x,t) > {\rm PSD_{max}}, \\ \dfrac{1}{\mu_{\rm PSD}(x,t)} & \text{otherwise.} \end{cases}$$

Here, $\rm PSD_{min}$ and $\rm PSD_{max}$ are the lower and upper bounds for the proportion of stopping distance (PSD), which represents the ratio between a vehicle's available spacing gap and its stopping distance at any given time, and $\mu_{\rm PSD}$ is the continuum approximation of the average PSD, developed in [21]:

$$\mu_{\rm PSD}(x,t) = 2b_{\rm comf}\frac{\rho_{\rm jam} - \rho}{\rho_{\rm jam}\rho V^2},$$

where $b_{\rm comf}$ is the maximum comfortable deceleration rate. Finally, $\mathfrak{L}_{\rm arr}$ and $\mathfrak{U}_{\rm arr}$ serve as the lower and upper bounds, respectively, defining the acceptable range of risk:

$$\begin{cases} \mathfrak{L}_{\rm arr} = \mathfrak{R}_{\rm perc}(\rho, V^L(\rho)), \quad V^L(\rho) = V_e\big(\rho(1+\delta_L)\big), \\ \mathfrak{U}_{\rm arr} = \mathfrak{R}_{\rm perc}(\rho, V^U(\rho)), \quad V^U(\rho) = V_e\big(\rho(1+\delta_U)\big), \end{cases}$$

where $V^L(\rho)$ and $V^R(\rho)$ represent the shifted speed-density curves compared to the equilibrium one. The constants δ_L and δ_U are subject to the condition $\delta_U < \delta_L$ in order to maintain the consistency condition $\mathfrak{L}$arr $\le \mathfrak{U}$arr.

The NET-RAT model can be rewritten in a vector form as

$$\boldsymbol{U}_t + \boldsymbol{F}(\boldsymbol{U})_x = B(\boldsymbol{U})\boldsymbol{U}_x + \boldsymbol{S}(\boldsymbol{U}), \tag{2}$$

where

$$\boldsymbol{U} = \begin{pmatrix} \rho \\ V \end{pmatrix}, \quad \boldsymbol{F} = \begin{pmatrix} \rho V \\ \dfrac{V^2}{2} \end{pmatrix}, \quad B(\boldsymbol{U}) = \begin{pmatrix} 0 & 0 \\ 0 & -\psi(\mathfrak{R}_{\rm perc})C(\rho) \end{pmatrix}, \quad \boldsymbol{S}(\boldsymbol{U}) = \begin{pmatrix} 0 \\ \dfrac{V_e(\rho) - V}{T_{\rm relax}} \end{pmatrix}. \tag{3}$$

The system (2)–(3) can be also recast in the following quasilinear form:

$$\boldsymbol{U}_t + \mathcal{A}(\boldsymbol{U})\boldsymbol{U}_x = \boldsymbol{S}(\boldsymbol{U}), \quad \mathcal{A}(\boldsymbol{U}) = \frac{\partial \boldsymbol{F}}{\partial \boldsymbol{U}} - B(\boldsymbol{U}) = \begin{pmatrix} V & \rho \\ 0 & \psi(\mathfrak{R}_{\rm perc})C(\rho) + V \end{pmatrix}. \tag{4}$$

3. Numerical Methods

In this section, we review the second-order FV PCCU and fifth-order FD A-WENO PCCU schemes for solving general non-conservative systems (2).

3.1. Second-Order Path-Conservative Central-Upwind Scheme

We first review the second-order FV PCCU scheme, which was introduced in [1] and then modified in [4].

We cover the computational domain with uniform cells $C_j := [x_{j-\frac{1}{2}}, x_{j+\frac{1}{2}}]$ of size Δx centered at $x_j = (x_{j-\frac{1}{2}} + x_{j+\frac{1}{2}})/2$. We assume that at a certain time $t \geq 0$, the computed solution, realized in terms of its cell averages

$$\overline{\boldsymbol{U}}_j(t) :\approx \frac{1}{\Delta x}\int\limits_{C_j} \boldsymbol{U}(x,t)\,\mathrm{d}x,$$

is available. For the sake of simplicity and conciseness, from now on, we will omit the explicit dependence on time for all of the indexed quantities.

The numerical solution is evolved in time by solving the following system of ODEs:

$$\frac{\mathrm{d}\overline{\boldsymbol{U}}_j}{\mathrm{d}t} = -\frac{1}{\Delta x}\left[\boldsymbol{\mathcal{F}}_{j+\frac{1}{2}} - \boldsymbol{\mathcal{F}}_{j-\frac{1}{2}} - \boldsymbol{B}_j - \frac{a^+_{j-\frac{1}{2}}}{a^+_{j-\frac{1}{2}} - a^-_{j-\frac{1}{2}}}\boldsymbol{B}_{\boldsymbol{\Psi},j-\frac{1}{2}} + \frac{a^-_{j+\frac{1}{2}}}{a^+_{j+\frac{1}{2}} - a^-_{j+\frac{1}{2}}}\boldsymbol{B}_{\boldsymbol{\Psi},j+\frac{1}{2}}\right] + \boldsymbol{S}(\overline{\boldsymbol{U}}_j), \tag{5}$$

where the CU numerical fluxes are given by

$$\boldsymbol{\mathcal{F}}_{j+\frac{1}{2}} = \frac{a^+_{j+\frac{1}{2}}\boldsymbol{F}(\boldsymbol{U}^-_{j+\frac{1}{2}}) - a^-_{j+\frac{1}{2}}\boldsymbol{F}(\boldsymbol{U}^+_{j+\frac{1}{2}})}{a^+_{j+\frac{1}{2}} - a^-_{j-\frac{1}{2}}} + \frac{a^+_{j+\frac{1}{2}}a^-_{j+\frac{1}{2}}}{a^+_{j+\frac{1}{2}} - a^-_{j+\frac{1}{2}}}\left(\boldsymbol{U}^+_{j+\frac{1}{2}} - \boldsymbol{U}^-_{j+\frac{1}{2}} - \boldsymbol{Q}_{j+\frac{1}{2}}\right). \tag{6}$$

Here, $\boldsymbol{U}^{\pm}_{j+\frac{1}{2}}$ are the right- and left-sided point values of $\boldsymbol{U}$ at the cell interface $x = x_{j+\frac{1}{2}}$ obtained by a piecewise linear reconstruction

$$\widetilde{\boldsymbol{U}}(x) = \overline{\boldsymbol{U}}_j + (\boldsymbol{U}_x)_j(x - x_j), \quad x \in C_j, \tag{7}$$

so that

$$\boldsymbol{U}^-_{j+\frac{1}{2}} = \overline{\boldsymbol{U}}_j + \frac{\Delta x}{2}(\boldsymbol{U}_x)_j, \quad \boldsymbol{U}^+_{j+\frac{1}{2}} = \overline{\boldsymbol{U}}_{j+1} - \frac{\Delta x}{2}(\boldsymbol{U}_x)_{j+1}. \tag{8}$$

In order to ensure the second order of accuracy of (8), the slopes $(\boldsymbol{U}_x)_j$ have to be at least first-order approximation of $\boldsymbol{U}_x(x_j,t)$. Moreover, the reconstruction (7) will be non-oscillatory provided $(\boldsymbol{U}_x)_j$ are computed using a nonlinear limiter. In our numerical experiments, we have utilized the minmod limiter; see, e.g., [28]:

$$(\boldsymbol{U}_x)_j = \mathrm{minmod}\left(\frac{\overline{\boldsymbol{U}}_j - \overline{\boldsymbol{U}}_{j-1}}{\Delta x}, \frac{\overline{\boldsymbol{U}}_{j+1} - \overline{\boldsymbol{U}}_j}{\Delta x}\right), \tag{9}$$

which is applied in the component-wise manner. Here, the minmod function is defined by

$$\mathrm{minmod}(z_1, z_2) := \frac{\mathrm{sign}(z_1) + \mathrm{sign}(z_2)}{2}\cdot\min\big(|z_1|, |z_2|\big). \tag{10}$$

The term $\boldsymbol{Q}_{j+\frac{1}{2}}$ given by

$$\boldsymbol{Q}_{j+\frac{1}{2}} = \mathrm{minmod}\left(\boldsymbol{U}^+_{j+\frac{1}{2}} - \boldsymbol{U}^*_{j+\frac{1}{2}}, \boldsymbol{U}^*_{j+\frac{1}{2}} - \boldsymbol{U}^-_{j+\frac{1}{2}}\right)$$

with

$$\boldsymbol{U}^*_{j+\frac{1}{2}} = \frac{a^+_{j+\frac{1}{2}}\boldsymbol{U}^+_{j+\frac{1}{2}} - a^-_{j+\frac{1}{2}}\boldsymbol{U}^-_{j+\frac{1}{2}} - \big\{\boldsymbol{F}(\boldsymbol{U}^+_{j+\frac{1}{2}}) - \boldsymbol{F}(\boldsymbol{U}^-_{j+\frac{1}{2}})\big\}}{a^+_{j+\frac{1}{2}} - a^-_{j+\frac{1}{2}}},$$

represents a "built-in" anti-diffusion term in the numerical flux (6); see [17] for the derivation of this term. The one-sided local speeds of propagation $a^{\pm}_{j+\frac{1}{2}}$ are estimated using the largest and smallest eigenvalues of $\mathcal{A}$: $\lambda_{\max}(\mathcal{A})$ and $\lambda_{\min}(\mathcal{A})$, for instance, by

$$\begin{aligned} a^+_{j+\frac{1}{2}} &= \max\Big\{\lambda_{\max}\big(\mathcal{A}(\boldsymbol{U}^+_{j+\frac{1}{2}})\big), \lambda_{\max}\big(\mathcal{A}(\boldsymbol{U}^-_{j+\frac{1}{2}})\big), 0\Big\},\\ a^-_{j+\frac{1}{2}} &= \min\Big\{\lambda_{\min}\big(\mathcal{A}(\boldsymbol{U}^+_{j+\frac{1}{2}})\big), \lambda_{\min}\big(\mathcal{A}(\boldsymbol{U}^-_{j+\frac{1}{2}})\big), 0\Big\}. \end{aligned} \tag{11}$$

Finally, the terms $\boldsymbol{B}_j$ and $\boldsymbol{B}_{\boldsymbol{\Psi},j+\frac{1}{2}}$ in (5) reflect the contributions of the non-conservative product terms inside the computational cell C_j and at the interface $x = x_{j+\frac{1}{2}}$, respectively:

$$\boldsymbol{B}_j :\approx \int\limits_{C_j} B(\boldsymbol{U}(x,t))\boldsymbol{U}_x(x,t)\,\mathrm{d}x, \quad \boldsymbol{B}_{\boldsymbol{\Psi},j+\frac{1}{2}} := \int\limits_0^1 B\big(\boldsymbol{\Psi}_{j+\frac{1}{2}}(s)\big)\frac{\mathrm{d}\boldsymbol{\Psi}_{j+\frac{1}{2}}(s)}{\mathrm{d}s}\,\mathrm{d}s. \tag{12}$$

Here, $\boldsymbol{B}_j$ is calculated by substituting $\widetilde{\boldsymbol{U}}(x)$ instead of $\boldsymbol{U}(x,t)$ and evaluating the resulting integral, and $\boldsymbol{B}_{\boldsymbol{\Psi},j+\frac{1}{2}}$ is computed using a path $\boldsymbol{\Psi}_{j+\frac{1}{2}}(s)$ connecting the left- and right-sided states $\boldsymbol{U}^-_{j+\frac{1}{2}}$ and $\boldsymbol{U}^+_{j+\frac{1}{2}}$. For details on evaluating (12), we refer the reader to [1].

3.2. Fifth-Order A-WENO Path-Conservative Central-Upwind Scheme

In this section, we provide a brief overview of the fifth-order A-WENO PCCU scheme introduced in [3]. Firstly, we restate the non-conservative system (2) in a quasi-conservative form:

$$\boldsymbol{U}_t + \boldsymbol{K}(\boldsymbol{U})_x = \boldsymbol{S}(\boldsymbol{U}), \quad \boldsymbol{K}\big(\boldsymbol{U}(x,t)\big) = \boldsymbol{F}\big(\boldsymbol{U}(x,t)\big) - \int\limits_{\widehat{x}}^{x} B\big(\boldsymbol{U}(\xi,t)\big)\boldsymbol{U}_x(\xi,t)\,\mathrm{d}\xi,$$

where $\boldsymbol{K}$ represents the global flux and $\widehat{x}$ is an arbitrary number. The numerical solution $\boldsymbol{U}_j \approx \boldsymbol{U}(x_j,t)$ is advanced in time by solving the following system of ODEs:

$$\begin{aligned}\frac{\mathrm{d}\boldsymbol{U}_j}{\mathrm{d}t} =& -\frac{1}{\Delta x}\left[\boldsymbol{\mathcal{F}}_{j+\frac{1}{2}} - \boldsymbol{\mathcal{F}}_{j-\frac{1}{2}} - \boldsymbol{B}_j - \frac{a^+_{j-\frac{1}{2}}}{a^+_{j-\frac{1}{2}} - a^-_{j-\frac{1}{2}}}\boldsymbol{B}_{\boldsymbol{\Psi},j-\frac{1}{2}} + \frac{a^-_{j+\frac{1}{2}}}{a^+_{j+\frac{1}{2}} - a^-_{j+\frac{1}{2}}}\boldsymbol{B}_{\boldsymbol{\Psi},j+\frac{1}{2}}\right]\\ &+ \frac{\Delta x}{24}\left[(\boldsymbol{K}_{xx})_{j+\frac{1}{2}} - (\boldsymbol{K}_{xx})_{j-\frac{1}{2}}\right] - \frac{7}{5760}(\Delta x)^3\left[(\boldsymbol{K}_{xxxx})_{j+\frac{1}{2}} - (\boldsymbol{K}_{xxxx})_{j-\frac{1}{2}}\right] + \boldsymbol{S}(\boldsymbol{U}_j),\end{aligned} \tag{13}$$

where $\boldsymbol{\mathcal{F}}_{j+\frac{1}{2}}$, $\boldsymbol{B}_j$, $\boldsymbol{B}_{\boldsymbol{\Psi},j+\frac{1}{2}}$, and $a^\pm_{j+\frac{1}{2}}$ are defined as in Section 3.1, but $\boldsymbol{U}^\pm_{j+\frac{1}{2}}$ are now calculated using the fifth-order WENO-Z interpolant applied to the local characteristic variables. The specific procedure for the WENO-Z interpolant from [14, 18, 30, 6, 8], can be found in [3, Appendix A], while the local characteristic decomposition for the NET-RAT traffic flow system is presented in Section 4.

Finally, the correction terms $(\boldsymbol{K}_{xx})_{j+\frac{1}{2}}$ and $(\boldsymbol{K}_{xxxx})_{j+\frac{1}{2}}$ are fourth- and second-order FD approximations of the spatial derivatives of $\boldsymbol{K}(\boldsymbol{U}(\cdot,t))$, respectively:

$$\begin{aligned}(\boldsymbol{K}_{xx})_{j+\frac{1}{2}} &= \frac{1}{48(\Delta x)^2}\left(-5\boldsymbol{K}_{j-2} + 39\boldsymbol{K}_{j-1} - 34\boldsymbol{K}_j - 34\boldsymbol{K}_{j+1} + 39\boldsymbol{K}_{j+2} - 5\boldsymbol{K}_{j+3}\right),\\ (\boldsymbol{K}_{xxxx})_{j+\frac{1}{2}} &= \frac{1}{2(\Delta x)^4}\left(\boldsymbol{K}_{j-2} - 3\boldsymbol{K}_{j-1} + 2\boldsymbol{K}_j + 2\boldsymbol{K}_{j+1} - 3\boldsymbol{K}_{j+2} + \boldsymbol{K}_{j+3}\right).\end{aligned}$$

Here, $\boldsymbol{K}_j = \boldsymbol{F}(\boldsymbol{U}_j) - \boldsymbol{I}_j$ and

$$\boldsymbol{I}_j :\approx \int\limits_{\widehat{x}}^{x_j} B\big(\boldsymbol{U}(\xi,t)\big)\boldsymbol{U}_x(\xi,t)\,\mathrm{d}\xi.$$

Notice that in order to achieve a fifth-order accuracy, it is necessary to evaluate the integral $\boldsymbol{I}_j$ and the integral in the term $\boldsymbol{B}_j$ in (12) using an (at least) fifth-order quadrature. In our numerical experiments, we have used the fifth-order Newton-Cotes quadrature from [3].

4. Study Design, Results, and Discussions

In this section, we apply the schemes from Section 3 to the NET-RAT model to investigate the performance of the PCCU schemes and shed light on certain behavioral aspects of the NET-RAT model. We test the second-order FV PCCU and fifth-order FD A-WENO PCCU schemes on several numerical examples and compare their performances. The tested schemes will be referred to as the 2-Order Scheme and 5-Order Scheme, respectively.

We numerically integrate the ODE systems (5) and (13) by the three-stage third-order strong stability preserving (SSP) Runge-Kutta method [see, e.g., 10, 9] and use the CFL number 0.5. The values of the parameters in the NET-RAT model borrowed from [23], are listed in Table 1.

Table 1: NET-RAT's parameter descriptions and the values adopted for numerical investigations. ARR stands for acceptable range of risk.

Parameter	**Description**	**Selected value**
$V_{\max}$	the maximum speed in the free-flow traffic	$1121/36\,(\mathrm{m/s})$
$\lvert C_{\mathrm{jam}}\rvert$	the magnitude of the propagation velocity $\lambda_* = V_e(\rho) + \rho V_e(\rho)$ under the jam condition (that is, at $\rho = \rho_{\mathrm{jam}}$)	$71/18\,(\mathrm{m/s})$
θ	shape parameter	10.04
$\rho_{\max}$	the maximum density	$0.11413\,(\mathrm{veh/m})$
T_{relax}	relaxation time	$40\,(\mathrm{s})$
$\mathrm{PSD}_{\min}$	the minimum practical value of PSD	0.2
$\mathrm{PSD}_{\max}$	the maximum practical value of PSD	5
b_{comf}	the maximum comfortable deceleration rate	4
γ_1	drivers' sensitivity to perceived risk below ARR	0.5
γ_2	drivers' sensitivity to perceived risk above ARR	1.052
δ_L	shape parameter that determines the lower boundary of ARR	**Variable**
δ_U	shape parameter that determines the lower boundary of ARR	**Variable**

4.1. Specifications of the PCCU Scheme for the NET-RAT Model

For the 2-Order Scheme, the point values $\rho^{\pm}_{j+\frac{1}{2}}$ and $V^{\pm}_{j+\frac{1}{2}}$ are computed using the piecewise linear minmod reconstruction (7)–(10).

For the 5-Order Scheme, we utilize the WENO-Z interpolation applied to the local characteristic variables, which are derived through the local characteristic decomposition. To this end, we first introduce

$$\mathcal{A}(\widehat{\boldsymbol{U}}_{j+\frac{1}{2}}) = \begin{pmatrix} \widehat{V}_{j+\frac{1}{2}} & \widehat{\rho}_{j+\frac{1}{2}} \\ 0 & \widehat{C}_{j+\frac{1}{2}}\widehat{\psi}_{j+\frac{1}{2}} + \widehat{V}_{j+\frac{1}{2}} \end{pmatrix},$$

where $\mathcal{A}$ is defined in (4), and

$$\widehat{\rho}_{j+\frac{1}{2}} = \frac{\rho_j + \rho_{j+1}}{2}, \quad \widehat{V}_{j+\frac{1}{2}} = \frac{\sqrt{\rho_j}\,V_j + \sqrt{\rho_{j+1}}\,V_{j+1}}{\sqrt{\rho_j} + \sqrt{\rho_{j+1}}},$$
$$\widehat{C}_{j+\frac{1}{2}} = \widehat{\rho}_{j+\frac{1}{2}} V_e'(\widehat{\rho}_{j+\frac{1}{2}}), \quad \widehat{\psi}_{j+\frac{1}{2}} = \psi\big(\mathfrak{R}_{\mathrm{perc}}(\widehat{\rho}_{j+\frac{1}{2}}, \widehat{V}_{j+\frac{1}{2}})\big).$$

The matrix $\mathcal{A}\big(\widehat{\boldsymbol{U}}_{j+\frac{1}{2}}\big)$ is then diagonalized with the help of the matrices

$$R_{j+\frac{1}{2}} = \begin{pmatrix} 1 & \dfrac{\widehat{\rho}_{j+\frac{1}{2}}}{\widehat{C}_{j+\frac{1}{2}}\widehat{\psi}_{j+\frac{1}{2}}} \\ 0 & 1 \end{pmatrix} \quad \text{and} \quad R^{-1}_{j+\frac{1}{2}} = \begin{pmatrix} 1 & -\dfrac{\widehat{\rho}_{j+\frac{1}{2}}}{\widehat{C}_{j+\frac{1}{2}}\widehat{\psi}_{j+\frac{1}{2}}} \\ 0 & 1 \end{pmatrix},$$

which are used to switch from and to the local characteristic variables. Namely, in the neighborhood of $x = x_{j+\frac{1}{2}}$, we introduce the local characteristic variables

$$\boldsymbol{\Gamma}_k = R^{-1}_{j+\frac{1}{2}}\boldsymbol{U}_k, \quad k = j-2, \ldots, j+3,$$

apply the WENO-Z interpolation to these six values of $\boldsymbol{\Gamma}$ to obtain the point values $\boldsymbol{\Gamma}^{\pm}_{j+\frac{1}{2}}$, and then switch back to the conservative variables

$$\boldsymbol{U}^{\pm}_{j+\frac{1}{2}} = R_{j+\frac{1}{2}}\boldsymbol{\Gamma}^{\pm}_{j+\frac{1}{2}}.$$

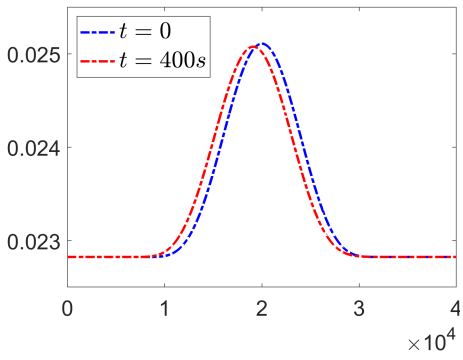

Figure 1: Accuracy test: Density (ρ) profiles at $t = 0$ and 400 s computed by the 2-Order scheme.

Equipped with the reconstructed point values $\rho^{\pm}_{j+\frac{1}{2}}$ and $V^{\pm}_{j+\frac{1}{2}}$, we estimate the one-sided local speeds of propagation by (11), which for the system (2)–(3) reduces to

$$a^+_{j+\frac{1}{2}} = \max\left\{V^+_{j+\frac{1}{2}}, V^-_{j+\frac{1}{2}}, 0\right\}, \quad a^-_{j+\frac{1}{2}} = \min\left\{V^+_{j+\frac{1}{2}} + \psi^+_{j+\frac{1}{2}} C^+_{j+\frac{1}{2}}, V^-_{j+\frac{1}{2}} + \psi^-_{j+\frac{1}{2}} C^-_{j+\frac{1}{2}}, 0\right\},$$

where $C^{\pm}_{j+\frac{1}{2}} = \rho^{\pm}_{j+\frac{1}{2}} V_e'(\rho^{\pm}_{j+\frac{1}{2}})$ and $\psi^{\pm}_{j+\frac{1}{2}} = \psi\big(\mathfrak{R}_{\text{perc}}(\rho^{\pm}_{j+\frac{1}{2}}, V^{\pm}_{j+\frac{1}{2}})\big)$.

4.2. Accuracy Test

This subsection is devoted to the experimental check of the numerical accuracy and rates of convergence of the proposed schemes. Before delving into the detailed analysis of the schemes' performance in handling discontinuities in various Riemann problems, it is crucial to first verify their performance on the initial value problem with smooth initial data and smooth solutions.

In the first numerical example, we demonstrate the experimental rates of convergence of the studied 2-Order and 5-Order Schemes. We consider the following smooth initial data:

$$\rho(x,0) = \frac{1+\varphi(x)}{5}\rho_{\max}, \quad V(x,0) = \frac{1+\varphi(x)}{5}V_{\max},$$
$$\varphi(x) = \begin{cases} \frac{1}{10}\sin^4\left[\frac{\pi}{24000}(x-8000)\right], & 8000 < x < 32000, \\ 0, & \text{otherwise}, \end{cases}$$

prescribed in the computational domain $[0, 40000]$ subject to free boundary conditions. We compute the numerical solution until the final time $t = 400$ s (at which the solution is still smooth; see Figure 1) using the 2-Order and 5-Order Schemes on a sequence of uniform meshes with $\Delta x = 40$, 20, 10, 5, and 5/2. We then estimate the L^1-errors and corresponding experimental convergence rates using the following Runge formulae, which are based on the solutions computed on three consecutive uniform grids with the mesh sizes Δx, $2\Delta x$, and $4\Delta x$ and denoted by $(\cdot)^{\Delta x}$, $(\cdot)^{2\Delta x}$, and $(\cdot)^{4\Delta x}$, respectively:

$$\text{Error}(\Delta x) \approx \frac{\delta_{12}^2}{|\delta_{12} - \delta_{24}|}, \quad \text{Rate}(\Delta x) \approx \log_2\left(\frac{\delta_{24}}{\delta_{12}}\right).$$

Here, $\delta_{12} := \|(\cdot)^{\Delta x} - (\cdot)^{2\Delta x}\|_{L^1}$ and $\delta_{24} := \|(\cdot)^{2\Delta x} - (\cdot)^{4\Delta x}\|_{L^1}$.

For the 5-Order Scheme, we select $\Delta t \sim \Delta x^{5/3}$, which balances the contribution of the temporal and spatial errors. The obtained results, reported in Table 2, clearly demonstrate that the experimental convergence rates correspond to the formal rates of the studied schemes.

4.3. Description of the Riemann Problems and Parameter Set-Up

This subsection presents the numerical test cases designed for the NET-RAT model, which will be used to evaluate the performance of the proposed numerical schemes. We begin our discussions by elaborating on the Riemann problem and specific properties of the NET-RAT model. To this end, let us consider the initial Riemann data of the form:

$$\boldsymbol{U}(x,0) = \begin{cases} \boldsymbol{U}_L & \text{if } x < x_0, \\ \boldsymbol{U}_R & \text{otherwise}, \end{cases} \tag{14}$$

Table 2: Accuracy test: L^1-errors and experimental convergence rates for ρ.

Δx	**2-Order Scheme**		**5-Order Scheme**	
	Error	**Rate**	**Error**	**Rate**
10	1.39e-4	1.98	2.44e-9	4.97
5	3.47e-5	1.99	7.60e-11	4.99
5/2	8.68e-6	1.99	2.60e-12	4.93

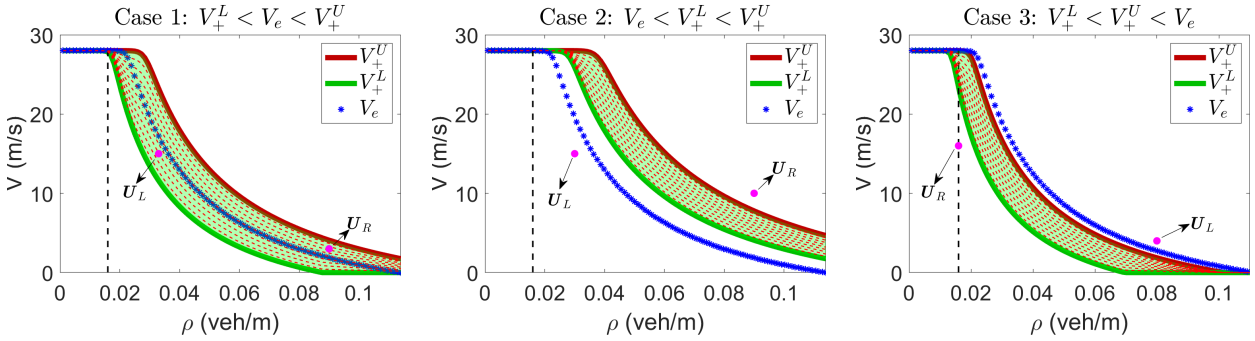

Figure 2: Three different possibilities for the status of the $\boldsymbol{U}_L$ and $\boldsymbol{U}_R$ in the speed-density plane.

where $\boldsymbol{U}_L$ and $\boldsymbol{U}_R$ represent the values of the state variables on the left and right sides of the discontinuity. Depending on the $\boldsymbol{U}_L$ and $\boldsymbol{U}_R$ values, several Riemann problem solution structures (combinations of shocks, rarefaction waves, and intermediate states) are possible.

Here, we present a range of numerical tests that represent qualitatively different Riemann problem solutions. It is important to emphasize that in the NET-RAT flow model, the solution structures for the Riemann problems are determined by multiple factors. These factors include the relative status of the state variables on both sides compared to the fundamental diagram, as well as the perception of risk not only on each side but also along the density range on the fundamental diagram.

To further elaborate, Figure 2 schematically shows three different possibilities (among others) for the status of $\boldsymbol{U}_L$ and $\boldsymbol{U}_R$ in the speed-density plane. These three cases have distinct properties which affect the solution structures.

For instance, in Case 1, both $\boldsymbol{U}_L$ and $\boldsymbol{U}_R$ are in areas bounded by the boundaries of the acceptable range of risk, where the risk perception parameters are also set such that the condition $V_+^L < V_e < V_+^U$ holds, where

$$V_+^L(\rho) = \max\left\{V^L(\rho), 0\right\}, \quad V_+^U(\rho) = \max\left\{V^U(\rho), 0\right\}.$$

In this case, $\psi(\mathfrak{R}_{\text{perc}}) = 1$ holds and the NET-RAT model becomes equivalent to a special case of the GSOM model family, that is, the model in [33] with a relaxation term, which can be written in the conservative form. In our recent work [3], we have shown that our proposed PCCU approach can solve the Riemann problem for the aforementioned GSOM model, and therefore, we will not consider the Riemann problems that correspond to Case 1.

In contrast, Riemann problems in Cases 2 and 3 are much more complicated as neither of $\boldsymbol{U}_L$ and $\boldsymbol{U}_R$ or the equilibrium states are within the boundaries of the acceptable range of risk. In such cases, solutions of the Riemann problems will inevitably contain multiple waves and intermediate states between left and right states.

In this work, we conduct comprehensive numerical tests that encompass both Case 2 and Case 3. With the model parameters in Table 1, we establish eight numerical tests, which are specified in Table 3.

4.4. Performance of the PCCU Schemes for the Riemann Problems

In this section, we apply the proposed numerical methods to solve the NET-RAT model using different risk perception parameters δ_L and δ_U for the eight test cases described in Table 3.

Table 3: Data for the eight Riemann problems (14).

Test	ρ_L	ρ_R	V_L	V_R	x_0	δ_L	δ_U
1	$0.3\rho_{\max}$	$0.3\rho_{\max}$	$V_e(\rho)-5$	$V_e(\rho)$	20000	0.2	0.1
2	$0.3\rho_{\max}$	$0.3\rho_{\max}$	$V_e(\rho)-5$	$V_e(\rho)$	20000	-0.2	-0.25
3	$0.3\rho_{\max}$	$0.3\rho_{\max}$	$V_e(\rho)+5$	$V_e(\rho)$	20000	0.1	0
4	$0.3\rho_{\max}$	$0.7\rho_{\max}$	$V_e(\rho)-5$	$V_e(\rho)+5$	20000	-0.1	-0.2
5	$0.85\rho_{\max}$	$0.2\rho_{\max}$	$V_e(\rho)+5$	$V_e(\rho)+5$	20000	-0.1	-0.2
6	$0.85\rho_{\max}$	$0.2\rho_{\max}$	$V_e(\rho)+5$	$V_e(\rho)+5$	20000	-0.2	-0.25
7	$0.85\rho_{\max}$	$0.2\rho_{\max}$	$V_e(\rho)+5$	$V_e(\rho)+5$	20000	-0.25	-0.3
8	$0.85\rho_{\max}$	$0.2\rho_{\max}$	$V_e(\rho)+2$	$V_e(\rho)-5$	20000	-0.2	-0.25

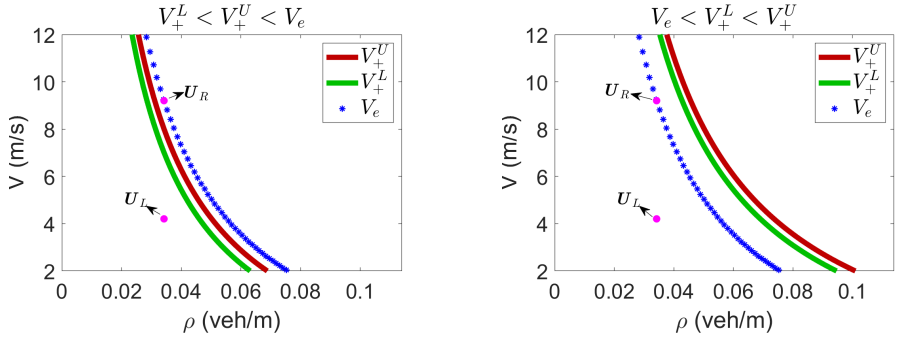

Figure 3: The states of $\boldsymbol{U}_L$ and $\boldsymbol{U}_R$ in the speed-density plane for Tests 1 (left) and 2 (right).

4.4.1. Solving the NET-RAT Model in the Absence of the Relaxation Term

We first investigate the solutions of the Riemann problems in the absence of the relaxation term $\frac{V_e(\rho)-V}{T_{\text{relax}}}$ in (1). The primary motivation for excluding the relaxation term in the previous sub-section was twofold:

(a) *The proposed PCCU schemes primarily focus on the treatment of nonlinear conservative terms.* By excluding the relaxation term, we can better assess the schemes' performance without the confounding effects that the relaxation term might introduce. These effects include dominating the schemes' performance near equilibrium states and altering solution structures and propagation near shocks and discontinuities;

(b) *In the NET-RAT model, the interplay between perceived risk and adaptation response time is primarily manifested in the characteristic waves.* By omitting the relaxation term, we can specifically investigate the portions of the macroscopic traffic waves that are generated by the nonlinear conservative terms, offering a clearer understanding of the influence of perceived risk on these particular wave components.

We compute the numerical results until the final time $t = 200\,\text{s}$ by both the 2-Order and 5-Order Schemes using 400 uniform cells in the computational domain $[0, 40000]$ subject to free boundary conditions. In Figures 4–11, we present the results, including the density and speed cross-sectional profiles at $t = 200\,\text{s}$. For each graph, we plot the results obtained using the 2-Order and 5-Order Schemes together with the reference solutions, which are computed by the 5-Order Scheme on a much finer mesh with 20000 uniform cells. As one can see, the PCCU schemes capture the solution structures of the comprehensive Riemann problems.

Let us now take a closer look at the results and shed light on physical and numerical implications of the obtained results. First, we observe that in all of the Tests, the solutions contain an intermediate state, which separates the left- and right-going waves: strong shocks and rarefactions, both in acceleration and deceleration situations. Additionally, contact discontinuities, at which the speed profile remains invariant across the density jump, appear in all of the Tests.

The PCCU schemes exhibit desirable performance in various aspects, with a notable focus on sharpness near shocks and contact discontinuities. Comparing the 2-Order and 5-Order Schemes, it is evident that the 5-Order Scheme outperforms its 2-Order counterpart, while both the 2-Order and 5-Order Schemes produce

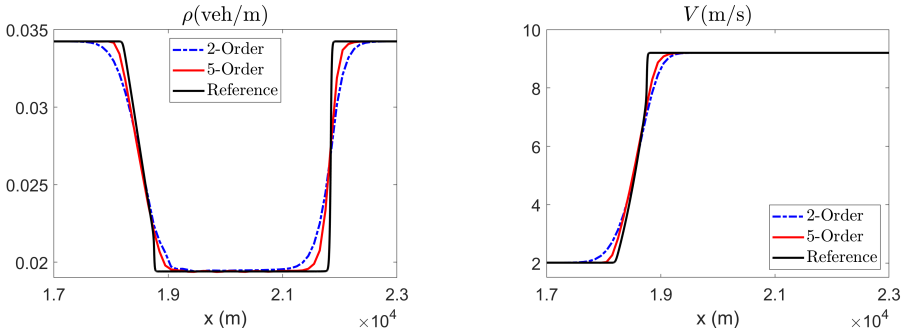

Figure 4: §4.4.1, Test 1: Density (left) and speed (right) computed by the 2-Order and 5-Order Schemes.

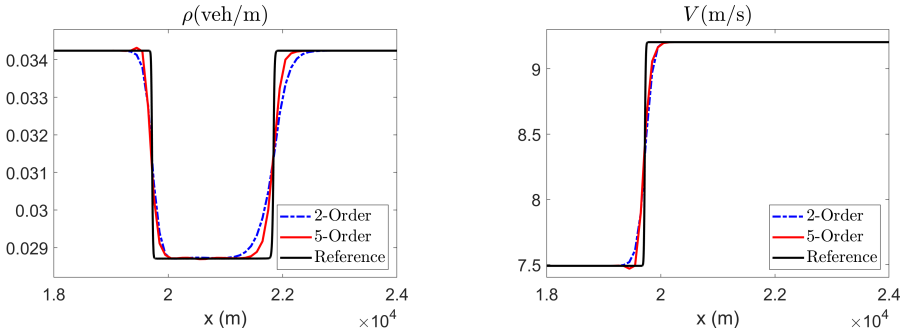

Figure 5: §4.4.1, Test 2: Same as in Figure 4.

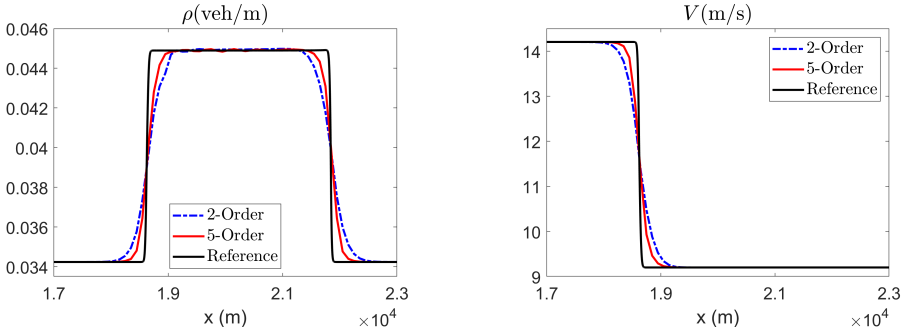

Figure 6: §4.4.1, Test 3: Same as in Figure 4.

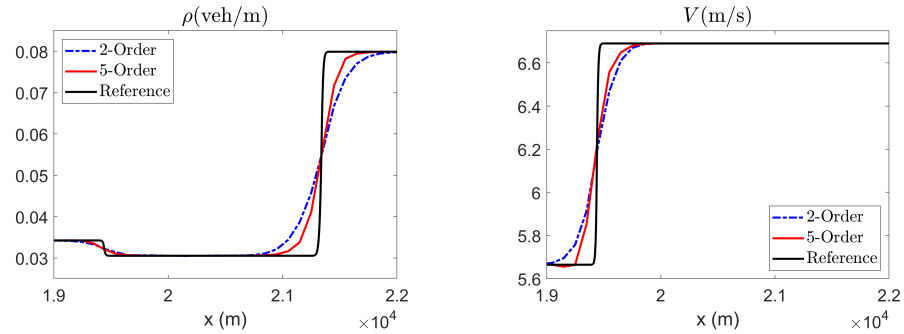

Figure 7: §4.4.1, Test 4: Same as in Figure 4.

almost non-oscillatory results.

Finally, let us briefly discuss how the PCCU schemes consistently reveal the impacts of risk perception in the NET-RAT model, particularly concerning the generation and propagation of characteristic waves in the absence of the relaxation term. When the perceived risk is below the acceptable range, drivers' sensitivity

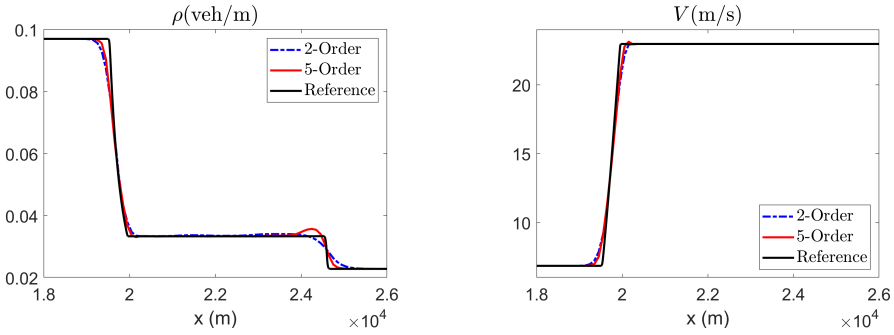

Figure 8: §4.4.1, Test 5: Same as in Figure 4.

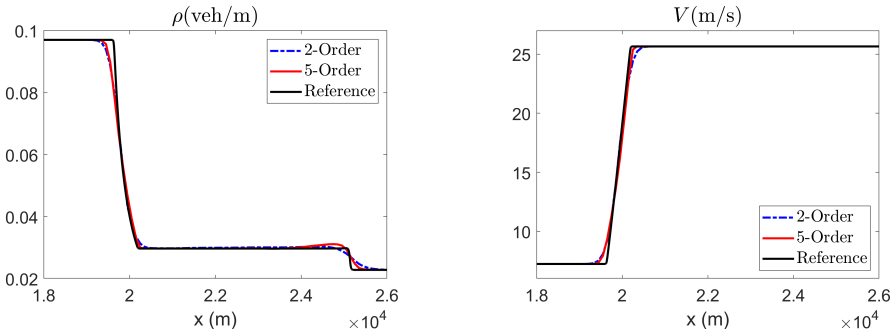

Figure 9: §4.4.1, Test 6: Same as in Figure 4.

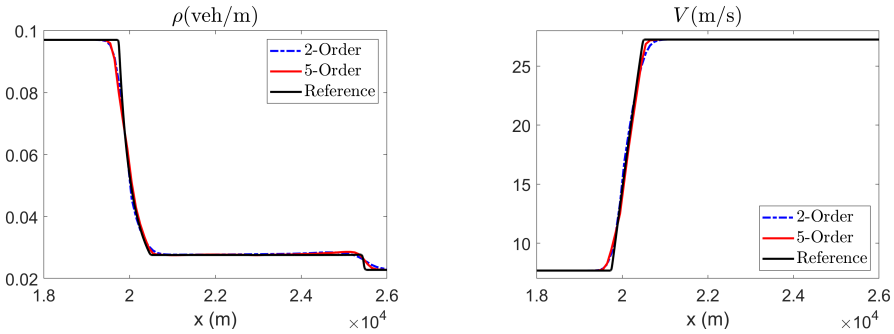

Figure 10: §4.4.1, Test 7: Same as in Figure 4.

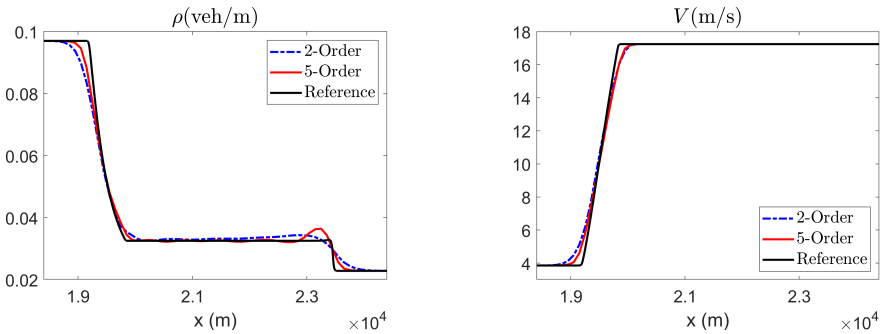

Figure 11: §4.4.1, Test 8: Same as in Figure 4.

to frontal stimuli is reduced, and as a result, drivers would take more time to respond and adapt to the changes in the traffic condition ahead. From a macroscopic perspective, this indicates that those components of the waves generated by the NET-RAT model, specifically the characteristic waves in the absence of the relaxation term, propagate slower. On the other hand, if the perceived risk is above the acceptable range,

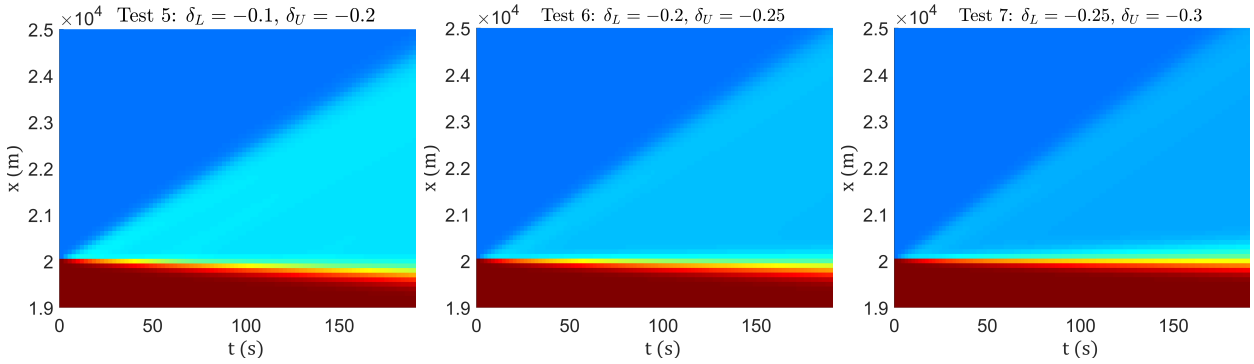

Figure 12: Spatio-temporal evolution of traffic density for Tests 5–7 with the same initial data but different risk perception parameters. With a decrease in δ_L and δ_U (from left to right), drivers' perception of risk and alertness increase, and they respond to the traffic conditions ahead quicker. Consequently, traffic waves propagate quicker.

drivers' sensitivity to frontal stimuli increases. Consequently, the characteristic waves of the NET-RAT model propagate more swiftly in response to the ahead traffic conditions.

The same observations apply to the changes in traffic density over time, as shown in Figure 12, when we vary the risk perception parameters (δ_L and δ_U) while keeping the same initial conditions. In this situation, it becomes evident that drivers with a heightened sense of risk perception are more attuned to the traffic conditions ahead. As a result, they react more swiftly, causing the waves on both sides of the intermediate state to propagate faster.

These properties are reflected in the results generated by the PCCU schemes. To elaborate, we consider Figure 3, which illustrates the left and right state variables compared to the boundaries of the acceptable range of risk in the speed-density plane for Tests 1 and 2. The corresponding solutions presented in Figures 4 and 5, respectively, show that for drivers whose perception of risk is lower (Test 2), the intermediate states span in a smaller region, compared to the case with higher risk perception (Test 1).

4.4.2. Solving the NET-RAT Model in the Presence of the Relaxation Term

In the previous subsection, we have numerically solved the Riemann problems for the NET-RAT model in the absence of the relaxation term: therefore the tests presented in Section 4.4.1 are rather academic. In practical scenarios, simulating the NET-RAT model with the relaxation term is essential for validating the proposed schemes' applicability in real-world situations. As in Section 4.4.1, we consider scenarios detailed in Table 3 and run the simulations up to time $t = 200\,\mathrm{s}$ using both the 2-Order and 5-Order Schemes on 400 uniform cells in the computational domain $[0, 40000]$ subject to free boundary conditions. For comparative analysis, reference solutions are obtained using the 5-Order Scheme on a finer grid of 20000 uniform cells, and the results, including density and speed profiles, are showcased in Figures 13–20.

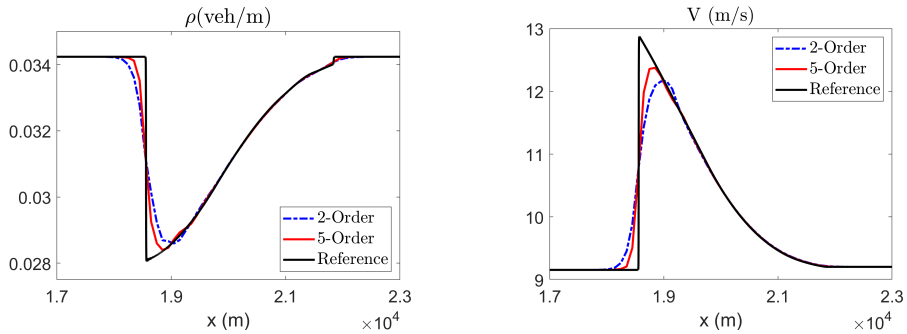

Figure 13: §4.4.2, Test 1: Density (left) and speed (right) computed by the 2-Order and 5-Order Schemes.

The obtained results show that the relaxation term significantly alters the solution structures in all of the Tests, particularly impacting the intermediate states that bridge the waves from the left and right sides of the initial discontinuity. When compared to the scenarios without the relaxation term shown in Figures 4–11, one can see that the relaxation term restricts the spatial development of the intermediate states, resulting in a quicker convergence of the waves.

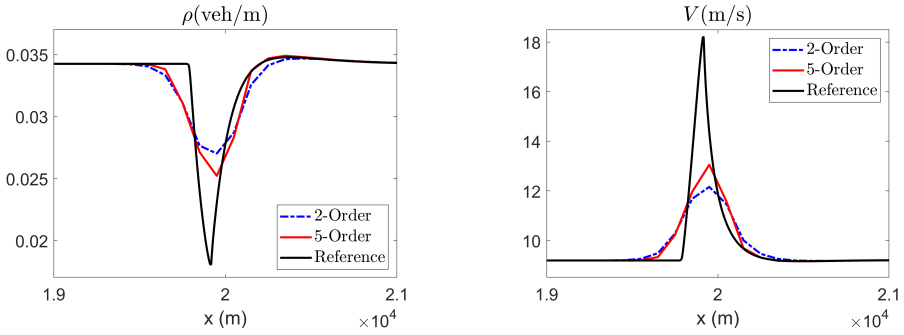

Figure 14: §4.4.2, Test 2: Same as in Figure 13.

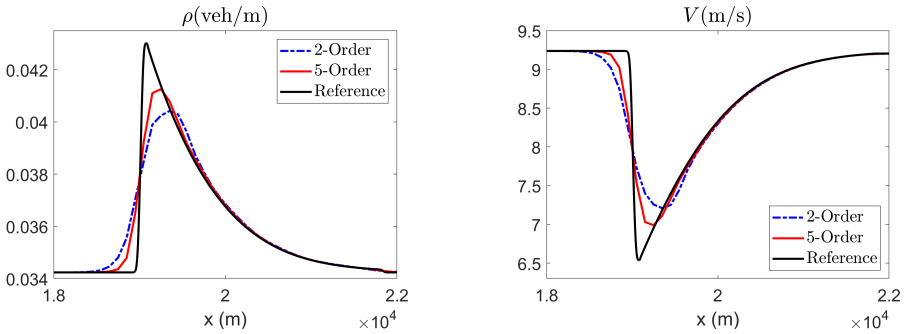

Figure 15: §4.4.2, Test 3: Same as in Figure 13.

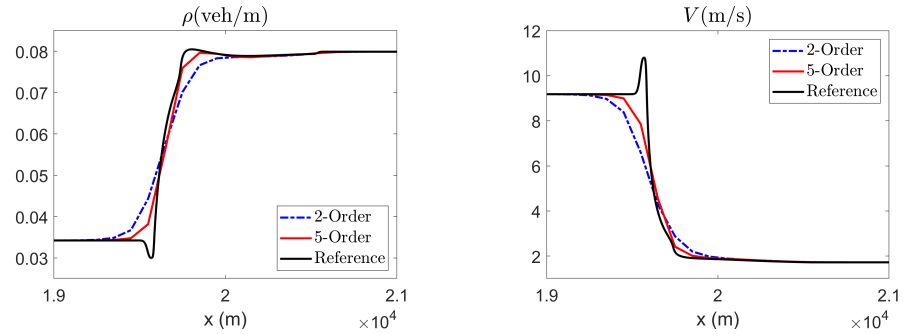

Figure 16: §4.4.2, Test 4: Same as in Figure 13.

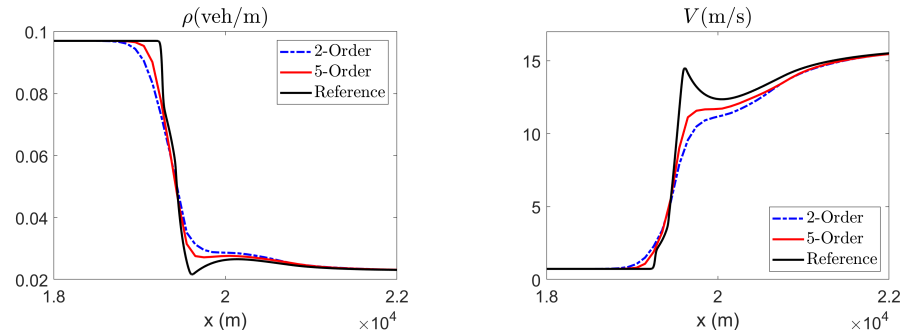

Figure 17: §4.4.2, Test 5: Same as in Figure 13.

Upon incorporating the relaxation term, it is evident that the proposed schemes are capable of capturing the overall solution structures in a range of test cases, where the solutions are composed of compounded waves including multiple shock waves, rarefaction waves, and contact discontinuities. Overall, the 5-Order Scheme markedly outperforms the 2-Order Scheme, particularly in regions where the intermediate states

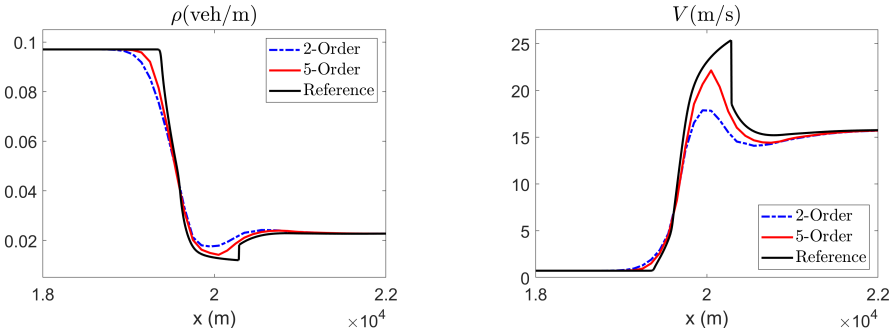

Figure 18: §4.4.2, Test 6: Same as in Figure 13.

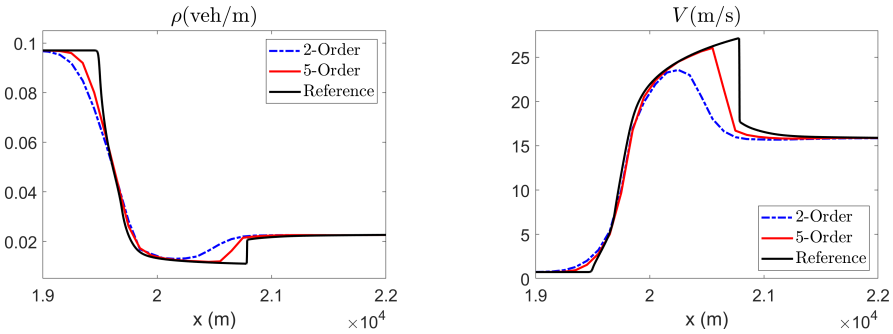

Figure 19: §4.4.2, Test 7: Same as in Figure 13.

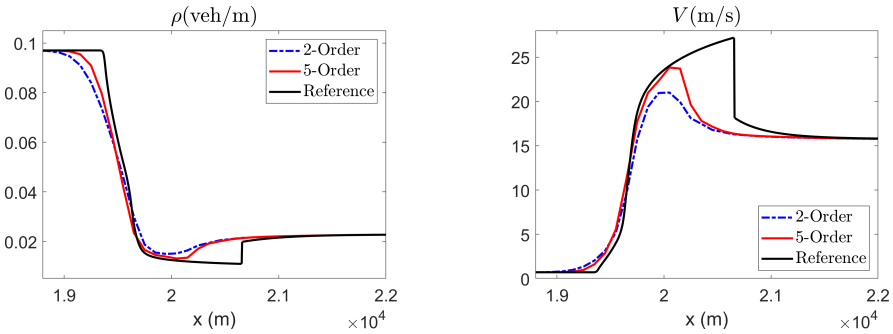

Figure 20: §4.4.2, Test 8: Same as in Figure 13.

are eliminated, and the waves on either side of the initial discontinuities quickly converge, as exemplified in Figures 13 and 20.

This phenomenon leads to a more noticeable accuracy gap between the reference solutions and the proposed schemes in these convergence zones. Such instances underscore the importance of selecting high-order spatial discretization schemes for accurately capturing complex traffic flow dynamics, as they offer pronounced justifications for their use in scenarios with rapidly converging waves and complex wave structures.

4.5. Periodic Initial Data

In this subsection, our analysis of the NET-RAT model's performance includes a simulation that introduces a slight disturbance into the otherwise stable and consistent traffic flow on a ring road with periodic boundary conditions.

To this end, we consider the well-known perturbation function in [12], and use the following initial condition:

$$\rho(x,0) = \rho_0 + \Delta\rho\sigma(x), \quad V(x,0) = V_e(\rho),$$
$$\sigma(x) = \begin{cases} \cosh^{-2}\left(\frac{x-4000}{W^+}\right) - \frac{W^+}{W^-}\cosh^{-2}\left(\frac{x-4000-\Delta x_0}{W^-}\right) & \text{if } x \le 3800, \\ \cosh^{-2}\left(\frac{x-7500}{W^+}\right) - \frac{W^+}{W^-}\cosh^{-2}\left(\frac{x-7500-\Delta x_0}{W^-}\right) & \text{otherwise,} \end{cases} \tag{15}$$

Table 4: Parameters for Tests 9–11 (15).

Test	ρ_0	δ_L	δ_U
9	$0.25\rho_{\max}$	0.3	0.2
10	$0.25\rho_{\max}$	0.1	0
11	$0.7\rho_{\max}$	-0.1	-0.2

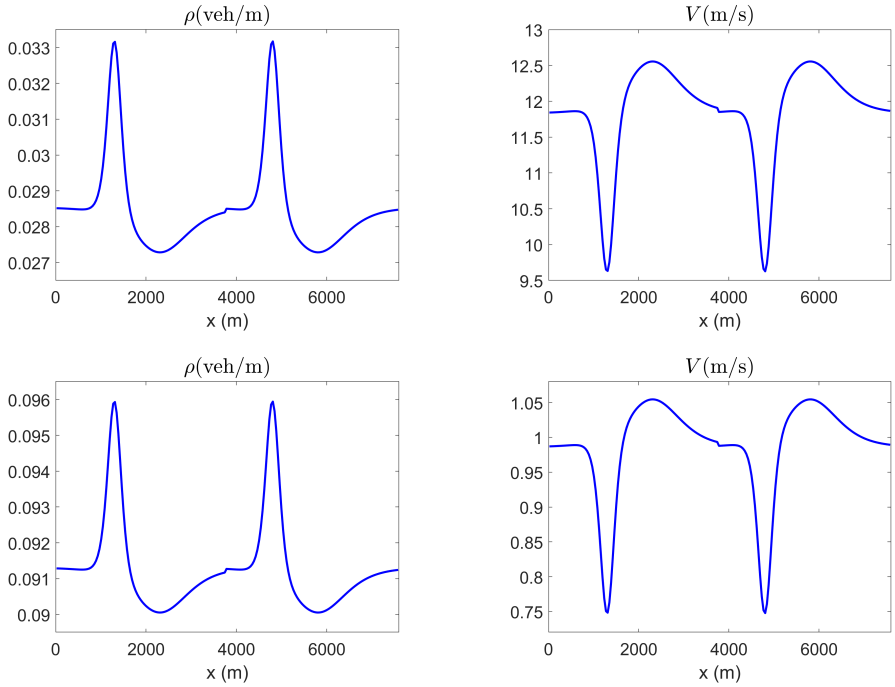

Figure 21: §4.5: Initial conditions for Tests 9 and 10 (top row) and Test 11 (bottom row).

subject to the periodic boundary conditions in the computational domain $[0, 7600]$.

Here, ρ_0 is the initially homogeneous density, $\Delta\rho$ is the amplitude of perturbation, Δx_0, W^-, and W^+ are spatial distances satisfying $\Delta x_0 = W^- + W^+$. In all numerical investigations, we set these as $W^+ = 201.25\,\text{m}$, $W^- = 805\,\text{m}$ and $\Delta\rho = 5\,(\text{veh/km})$.

In general, the scenarios of the form (15) are commonly used for examining how the model handles the emergence and spread of traffic instabilities starting from a uniformly stable traffic condition. In our examples, we specifically choose these test cases as they facilitate the creation of bumps and deep troughs in the density profiles, making them ideal for evaluating the relative effectiveness of the 2-Order and 5-Order Schemes. Our primary focus is, however, on stable traffic conditions, where achieving convergence is feasible, and thus, meaningful comparison can be made across the numerical results obtained by the 2-Order and 5-Order Schemes, as well as against the reference solutions.

We design several numerical tests as in Table 4 to investigate the performance of the proposed PCCU schemes under various stability conditions of NET-RAT (see [23] for more discussions on the stability criteria of the NET-RAT model). The initial conditions for these test cases are illustrated in Figure 21.

We compute the numerical solutions until either time $t = 500\,\text{s}$ (Test 9) or $t = 9000\,\text{s}$ (Tests 10 and 11) by both the 2-Order and 5-Order Schemes on 200 uniform cells and present the obtained results in Figures 22–24 together with the corresponding reference solution computed by the 2-Order Scheme on a much finer mesh with 4000 uniform cells.

The developed PCCU schemes effectively capture the solution structures in a non-oscillatory manner, with the 5-Order Scheme showing a marked improvement in resolution over the 2-Order Scheme.

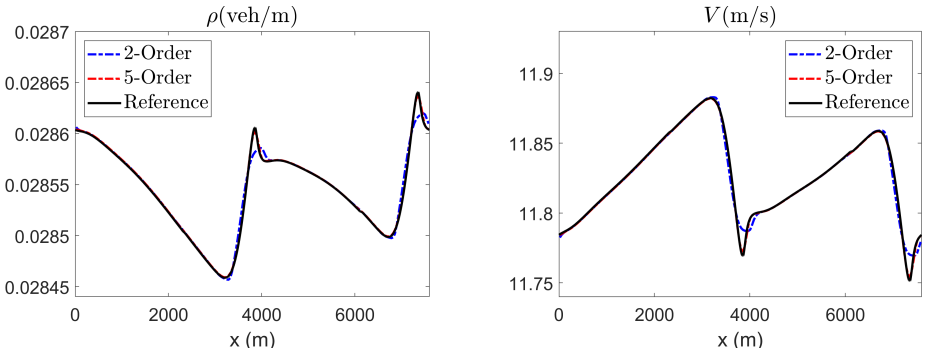

Figure 22: §4.5, Test 9: Density (left) and speed (right) computed by the 2-Order and 5-Order Schemes.

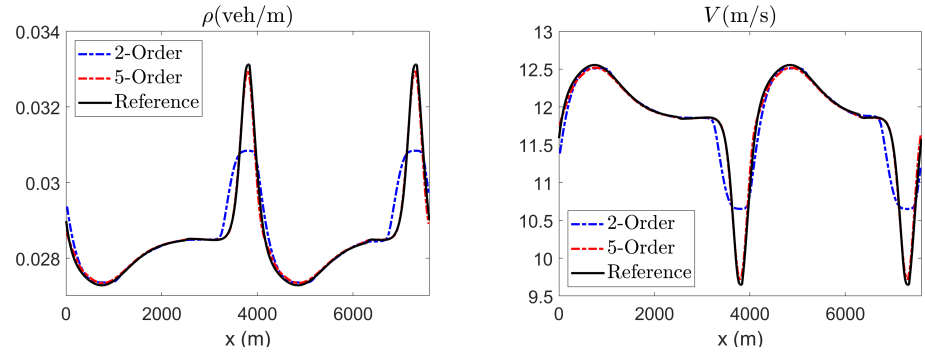

Figure 23: §4.5, Test 10: Same as in Figure 22.

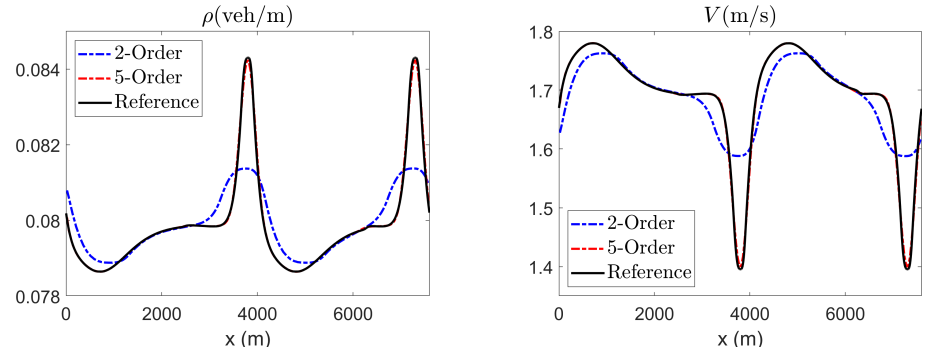

Figure 24: §4.5, Test 11: Same as in Figure 22.

5. Conclusion

Non-equilibrium ("second-order") hyperbolic traffic models can be obtained through continuum approximations of car-following models. However, the incorporation of complex human factors in these car-following models can cause the resulting hyperbolic traffic model to lose its conservative property. Consequently, obtaining numerical solutions near discontinuities becomes challenging due to the presence of non-conservative product terms.

This issue is also pertinent to the recently developed behavioral NET-RAT model, as presented in [23]. In this model, drivers' perception of risk is incorporated based on car-following information, impacting their sensitivity to changes in the traffic conditions ahead. The interaction between drivers' response to the perceived risk is modeled using the well-known risk allostasis theory [7].

In order to overcome numerical difficulties, we have introduced the path-conservative approach and developed second-order path-conservative central-upwind (PCCU) scheme. We have also extended the proposed PCCU scheme to the fifth-order of accuracy using the alternative weighted essentially non-oscillatory (A-WENO) framework to obtain the A-WENO PCCU scheme. The proposed schemes have been applied to multiple test cases with strong shocks and intermediate states emerging between initial discontinuities on

both sides. For each test case, we compare the performance of the proposed fifth- and second-order PCCU schemes.

Initially, we have studied the proposed PCCU schemes on the NET-RAT model without the relaxation term, focusing solely on the characteristic speed-induced waves. The numerical results demonstrate that the fifth-order A-WENO PCCU scheme captures the overall solution structures and different types of waves, such as shocks, rarefactions, and contact discontinuities, significantly better than the second-order PCCU scheme.

In the next step, we have incorporated the relaxation term into the model and conducted simulations for all of the test cases using the proposed PCCU schemes. The results showed that the presence of the relaxation term leads to the dissipation of the multi-fold waves arising from the discontinuities. Despite this, the proposed fifth-order A-WENO PCCU scheme still showed significant improvements over its second-order counterpart in terms of prediction accuracy.

The NET-RAT model has the potential to more accurately and reliably predict traffic states, if it is rigorously calibrated and validated on real-world traffic scenarios. Such work is currently ongoing.

Acknowledgements

This research was partially funded by the Australian Research Council (ARC) through the Discover Project (DP210102970) and Dr. Zuduo Zheng's Discovery Early Career Researcher Award (DECRA; DE160100449). The work of A. Kurganov was supported in part by NSFC grant 12171226, and by the fund of the Guangdong Provincial Key Laboratory of Computational Science and Material Design (No. 2019B030301001).

References

[1] M. J. Castro Díaz, A. Kurganov, and T. Morales de Luna. Path-conservative central-upwind schemes for non-conservative hyperbolic systems. *ESAIM Math. Model. Numer. Anal.*, 53(3):959–985, 2019.

[2] D. Chen, J. A. Laval, S. Ahn, and Z. Zheng. Microscopic traffic hysteresis in traffic oscillations: A behavioral perspective. *Transport. Res. B-Meth.*, 46(10):1440–1453, 2012.

[3] S. Chu, A. Kurganov, S. Mohammadian, and Z. Zheng. Fifth-order A-WENO path-conservative central-upwind scheme for behavioral non-equilibrium traffic models. *Commun. Comput. Phys.*, 33(3):692–732, 2023.

[4] S. Chu, A. Kurganov, and M. Na. Fifth-order A-WENO schemes based on the path-conservative central-upwind method. *J. Comput. Phys.*, 469, 2022. Paper No. 111508.

[5] J. M del Castillo. Three new models for the flow-density relationship: derivation and testing for freeway and urban data. *Transportmetrica*, 8(6):443–465, 2012.

[6] W. S. Don, D.-M. Li, Z. Gao, and B.-S. Wang. A characteristic-wise alternative WENO-Z finite difference scheme for solving the compressible multicomponent non-reactive flows in the overestimated quasi-conservative form. *J. Sci. Comput.*, 82(2), 2020. Paper No. 27.

[7] R. Fuller. Driver control theory: From task difficulty homeostasis to risk allostasis. In *Handbook of traffic psychology*, pages 13–26. Elsevier, 2011.

[8] Z. Gao, L.-L. Fang, B.-S. Wang, Y. Wang, and W. S. Don. Seventh and ninth orders alternative WENO finite difference schemes for hyperbolic conservation laws. *Comput. & Fluids*, 202(1), 2020. Paper No. 104519.

[9] S. Gottlieb, D. Ketcheson, and C.-W. Shu. *Strong stability preserving Runge-Kutta and multistep time discretizations*. World Scientific Publishing Co. Pte. Ltd., Hackensack, NJ, 2011.

[10] S. Gottlieb, C.-W. Shu, and E. Tadmor. Strong stability-preserving high-order time discretization methods. *SIAM Rev.*, 43(1):89–112, 2001.

[11] D. Helbing. Traffic and related self-driven many-particle systems. *Rev. Mod. Phys.*, 73(4), 2001. Paper No. 1067.

[12] D. Helbing and M. Treiber. Numerical simulation of macroscopic traffic equations. *Comput. Sci. Eng.*, 1(5):89–98, 1999.

[13] R. Jiang, Q. Wu, and Z. Zhu. Full velocity difference model for a car-following theory. *Phys. Rev. E*, 64(1), 2001. Paper No. 017101.

[14] Y. Jiang, C.-W. Shu, and M. P. Zhang. An alternative formulation of finite difference weighted ENO schemes with Lax-Wendroff time discretization for conservation laws. *SIAM J. Sci. Comput.*, 35(2):A1137–A1160, 2013.

[15] W. Jin and H. M. Zhang. Solving the Payne-Whitham traffic flow model as a hyperbolic system of conservation laws with relaxation. *Transp. Sci.*, 1, 2001. Paper No. 24.

[16] W.-L. Jin. On the equivalence between continuum and car-following models of traffic flow. *Transport. Res. B-Meth.*, 93:543–559, 2016.

[17] A. Kurganov and C.-T. Lin. On the reduction of numerical dissipation in central-upwind schemes. *Commun. Comput. Phys.*, 2(1):141–163, 2007.

[18] H. Liu. A numerical study of the performance of alternative weighted ENO methods based on various numerical fluxes for conservation law. *Appl. Math. Comput.*, 296:182–197, 2017.

[19] S. Mammar, J.-P. Lebacque, and H. H. Salem. Riemann problem resolution and Godunov scheme for the Aw-Rascle-Zhang model. *Transport. Sci.*, 43(4):531–545, 2009.

[20] S. Mohammadian. *Freeway traffic flow dynamics and safety: A behavioural continuum framework.* PhD thesis, Queensland University of Technology, 2021.

[21] S. Mohammadian, M. M. Haque, Z. Zheng, and A. Bhaskar. Integrating safety into the fundamental relations of freeway traffic flows: A conflict-based safety assessment framework. *Anal. Methods Accid. Res.*, 32, 2021. Paper No. 100187.

[22] S. Mohammadian, A. M. Moghaddam, and A. Sahaf. On the performance of HLL, HLLC, and Rusanov solvers for hyperbolic traffic models. *Comput. & Fluids*, 231, 2021. Paper No. 105161.

[23] S. Mohammadian, Z. Zheng, M. Haque, and A. Bhaskar. NET-RAT: Non-equilibrium traffic model based on risk allostasis theory. *Transport. Res. A-Pol.*, 174, 2023. Paper No. 103731.

[24] S. Mohammadian, Z. Zheng, M. M. Haque, and A. Bhaskar. Continuum modeling of freeway traffic flows: State-of-the-art, challenges and future directions in the era of connected and automated vehicles. *Commun. Transp. Res.*, 3, 2023. Paper No. 100107.

[25] Saeed Mohammadian, Zuduo Zheng, Md Mazharul Haque, and Ashish Bhaskar. Performance of continuum models for realworld traffic flows: Comprehensive benchmarking. *Transport. Res. B-Meth.*, 147:132–167, 2021.

[26] M. Papageorgiou. Some remarks on macroscopic traffic flow modelling. *Transport. Res. A-Pol.*, 32(5):323–329, 1998.

[27] M. Saifuzzaman, Z. Zheng, M. M. Haque, and S. Washington. Understanding the mechanism of traffic hysteresis and traffic oscillations through the change in task difficulty level. *Transport. Res. B-Meth.*, 105:523–538, 2017.

[28] P. K. Sweby. High resolution schemes using flux limiters for hyperbolic conservation laws. *SIAM J. Numer. Anal.*, 21(5):995–1011, 1984.

[29] M. Treiber and A. Kesting. *Traffic Flow Dynamics: Data, Models and Simulation.* Springer-Verlag, Berlin, Heidelberg, 2013.

[30] B.-S. Wang, P. Li, Z. Gao, and W. S. Don. An improved fifth order alternative WENO-Z finite difference scheme for hyperbolic conservation laws. *J. Comput. Phys.*, 374(1):469–477, 2018.

[31] Y. Wang, X. Yu, J. Guo, I. Papamichail, M. Papageorgiou, L. Zhang, S. Hu, Y. Li, and J. Sun. Macroscopic traffic flow modelling of large-scale freeway networks with field data verification: State-of-the-art review, benchmarking framework, and case studies using METANET. *Transport. Res. C-Emer.*, 145, 2022. Paper No. 103904.

[32] H. M. Zhang. Structural properties of solutions arising from a nonequilibrium traffic flow theory. *Transport. Res. B-Meth.*, 34(7):583–603, 2000.

[33] H. M. Zhang. Driver memory, traffic viscosity and a viscous vehicular traffic flow model. *Transport. Res. B-Meth.*, 37(1):27–41, 2003.